ADVANCED FUNCTIONAL MATERIALS
www.afm-journal.de

Surface Chemistry Dictates the Osteogenic and Antimicrobial Properties of Palladium-, Platinum-, and Titanium-Based Bulk Metallic Glasses

William A. Lackington, Romy Wiestner, Elena Pradervand, Peter Schweizer, Flavia Zuber, Qun Ren, Mihai Stoica, Jörg F. Löffler, and Markus Rottmar**

Titanium alloys are commonly used as biomaterials in musculoskeletal applications, but their long-term efficacy can be limited by wear and corrosion, stress shielding, and bacterial colonization. As a promising alternative, bulk metallic glasses (BMGs) offer superior strength and corrosion resistance, but the influence of their chemical composition on their bioactivity remains largely unexplored. This study, therefore, aims to examine how the surface chemistry of palladium (Pd)-, platinum (Pt)-, and titanium (Ti)-based BMGs can steer their response to biological systems. The chemical composition of BMGs governs their thermophysical and mechanical properties, with Pd-based BMGs showing exceptional glass-forming ability suitable for larger implants, and all BMGs exhibiting a significantly lower Young's modulus than Ti-6Al-4 V (Ti64), suggesting a potential to reduce stress shielding. Although BMGs feature copper depletion at the near surface, their surface chemistry remains more stable than that of Ti64 and supports blood biocompatibility. Fibrin network formation is heavily dependent on BMGs' chemical composition and Ti-based BMGs support thicker fibrin network formation than Ti64. Furthermore, BMGs outperform Ti64 in promoting mineralization of human bone progenitor cells and demonstrate antimicrobial properties against *Staphylococcus aureus* in a surface chemistry-dependent manner, thereby indicating their great potential as biomaterials for musculoskeletal applications.

1. Introduction

Metallic alloys are the most widely used class of biomaterials in musculoskeletal applications. Titanium (Ti) and Ti-alloys, including Ti-6Al-4 V (Ti64), represent the gold standard in dental and orthopedic implants due to their high strength and good biocompatibility.[1] However, implant failure remains a challenge whereby both mechanical and biological issues need to be addressed. Ti64 implants can exhibit wear and may have issues with respect to the release of aluminum and vanadium,[2–4] which are potentially harmful to human health.[5,6] Furthermore, the mismatch between the Young's modulus of Ti64 implants and cortical bone, which can be even greater in osteoporotic patients, can lead to stress shielding of the bone and ultimately to aseptic loosening of the implant.[7,8] Additionally, the surface of Ti64, like that of many other implants with no antimicrobial properties, can give rise to a so-called "race-for-the-surface"—a competition between host–cell integration and bacterial colonization.[9–11]

W. A. Lackington, R. Wiestner, E. Pradervand, F. Zuber, Q. Ren, M. Rottmar
Biointerfaces Lab, Empa
Swiss Federal Laboratories for Materials Science and Technology
9014 St. Gallen, Switzerland

R. Wiestner, E. Pradervand, M. Stoica, J. F. Löffler
Laboratory of Metal Physics and Technology, Department of Materials
ETH Zurich
8093 Zurich, Switzerland

P. Schweizer
Mechanics of Materials & Nanostructures Lab, Empa
Swiss Federal Laboratories for Materials Science and Technology
3603 Thun, Switzerland

The ORCID identification number(s) for the author(s) of this article can be found under https://doi.org/10.1002/adfm.202302069

DOI: 10.1002/adfm.202302069

Although various surface coatings, which aim to prevent bacterial adhesion, have been developed, they generally suffer from a lack of stability, delamination upon implantation, and limited bioactivity.[12,13] These limitations have motivated the search for alternative implant materials that support osseointegration while also providing sustained antimicrobial activity.

Bulk metallic glasses (BMGs) have received increasing interest as potential alternatives to Ti64 owing to their unique mechanical properties.[14] Their amorphous structure, characterized by a lack of grain- and phase-boundaries, renders BMGs with superior wear resistance, good corrosion resistance,[5,15,16] a lower Young's modulus,[17] and enhanced strength in comparison to crystalline Ti64.[6,18] While the use of Ti64 and other crystalline materials offers broad versatility in musculoskeletal applications, ranging from small dental implants to larger hip replacements, BMGs have traditionally been limited by their comparably low critical casting thickness. However, the development of new alloys with enhanced glass-forming ability has led to a steady increase of critical casting thickness over time,[19–21] including Ti-based (6 mm) [22] and platinum (Pt)-based (4 mm) [23] BMGs. Such alloys may be best suited toward smaller implant parts such as dental implants and plate fixation screws, while palladium (Pd)-based (72 mm) compositions might be suitable for bulkier applications including fixation plates and prostheses.[21]

The majority of BMG research has focused on the optimization of alloy compositions in order to enhance their thermophysical and mechanical properties.[24] However, less is known about how the composition of BMGs can steer their bioactivity. The potential use of BMGs for blood-contacting devices was recently reported, showing that $Pd_{77.5}Si_{16.5}Cu_6$ exhibits higher thrombogenic resistance than Ti64 in vitro,[25] indicating that the thrombogenic properties of BMGs, and thus their application, can be tailored based on their chemical composition. In another study, $Pt_{57.5}Cu_{14.7}Ni_{5.3}P_{22.5}$ showed comparable performance to Ti64 in a load-bearing transcortical model of osseointegration in mice.[26] However, it remains unclear how changes in the composition of BMGs can influence bone mineralization, as the Pt-based BMG was investigated mainly because of its superior thermoplastic processability, rather than its composition. Another class of BMGs features titanium as the dominant element to take advantage of its biocompatibility.[17] In relation to this, $Ti_{40}Zr_{10}Cu_{36}Pd_{14}$ was recently shown to support human gingival fibroblast attachment and proliferation, and owing to the formation of a copper oxide layer, the Ti-based BMG was additionally found to exhibit antibacterial activity against *A. actinomycetemcomitans*.[14] Collectively, these reports suggest that the biological response to BMGs can be steered by their surface chemistry, although it remains unclear how dynamic (or stable) the surface chemistry of BMGs can be in a biological environment.

This study, therefore, aimed to demonstrate that the influence of BMGs on biological systems is dependent on the composition and stability of their surface chemistry. To test this hypothesis, we investigated how varying BMG compositions could influence the interactions with blood, the osteogenic differentiation of human bone progenitor cells (HBCs), and the antimicrobial activity against *Staphylococcus aureus (S. aureus)*, in comparison to crystalline Ti64. Reflecting compositions with a wide range of critical casting thickness, BMGs based on Pd ($Pd_{43}Cu_{27}Ni_{10}P_{20}$), Pt ($Pt_{57.4}Cu_{14.7}Ni_{5.3}P_{22.6}$), and Ti ($Ti_{40}Zr_{10}Cu_{36}Pd_{14}$, $Ti_{40}Zr_{10}Cu_{32}Pd_{14}Ga_4$, and $Ti_{40}Zr_{10}Cu_{32}Pd_{14}Sn_4$)[27] were assessed. Notably, all BMG compositions included copper, which has well-established dose-dependent antimicrobial properties.[28] Prior to investigating their bioactivity, the thermal processability of all BMGs was assessed after preparation and their amorphousness was evaluated using X-ray diffraction (XRD) and transmission electron microscopy (TEM). Furthermore, comparing newly prepared samples with 1-month-aged samples, the stability of their near-surface structure was characterized by TEM. Taken together, this study presents a case for the use of BMGs in dental and orthopedic applications, where their material properties and chemical composition can be exploited to stimulate superior responses in comparison to traditionally used crystalline alloys.

2. Experimental Section

2.1. Sample Preparation

Crystalline Ti-6Al-4 V (in wt%, $Ti_{86}Al_{10}V_4$ in at%) was purchased (Titan Grade 5, Ti6Al4V (ELI), ISO 5832-3, L. Klein SA, Switzerland) as cylindrical rods with 5 mm diameter. Pd-based ($Pd_{43}Cu_{27}Ni_{10}P_{20}$) and Pt-based ($Pt_{57.4}Cu_{14.7}Ni_{5.3}P_{22.6}$) BMGs were also purchased (PX Group SA, Switzerland) as cylindrical rods with 5 and 6 mm diameter, respectively. Ti-based ($Ti_{40}Zr_{10}Cu_{36}Pd_{14}$, $Ti_{40}Zr_{10}Cu_{32}Pd_{14}Sn_4$, and $Ti_{40}Zr_{10}Cu_{32}Pd_{14}Ga_4$) BMGs were prepared by alloying lumps of pure elements (purity > 99.9%, Sn > 99%) in an Arc Melter AM 200 (Edmund Bühler GmbH, Germany) with 6.0 (99.9999% purity) argon atmosphere. The Ti-based master alloy ingots were remelted five times in order to ensure a homogenous composition. The Pt-based and Ti-based BMG rods were prepared by remelting a small mass (i.e., 9 and 5 grams, respectively) of the corresponding alloys in a Compact Arc Melter MAM-1 (Edmund Bühler GmbH) in 6.0 argon atmosphere and subsequent suction casting. In this way, 3 cm long cylindrical rods with 5 mm diameter were obtained. $Ti_{40}Zr_{10}Cu_{32}Pd_{14}Ga_4$ BMG was cast to discs of 5 mm diameter and 1 mm thickness. The casting parameters, including temperature and duration of heat exposure, were varied for the different alloy compositions. All materials were cut into either 1- or 2-mm thick discs and polished (RotoPol-21, Struers, Germany) until mirror-like appearance (roughness 0.05 µm) with Al_2O_3 MasterPrep Suspension (Buehler, USA). The last step was performed shortly before the use of the materials in experiments, and involved further polishing of the surfaces with a water-based silica polishing suspension to a surface finish of 0.02 µm, followed by ultrasonic cleaning in isopropanol and then in deionized water (dH_2O) for 15 min, as previously described.[25] A list of BMGs investigated in this study, in addition to the crystalline comparison, is presented in **Table 1**. To assess how aging influences the near-surface structure, samples were aged in de-ionized water for 30 days at 37 °C.

Table 1. Composition of BMGs investigated in this study. The BMGs were compared to crystalline Ti64 (Ti-6Al-4 V in wt%, $Ti_{86}Al_{10}V_4$ in at%).

Composition [at%]	Abbreviation
$Pd_{43}Cu_{27}Ni_{10}P_{20}$	Pd
$Pt_{57.4}Cu_{14.7}Ni_{5.3}P_{22.6}$	Pt
$Ti_{40}Zr_{10}Cu_{36}Pd_{14}$	Ti
$Ti_{40}Zr_{10}Cu_{32}Pd_{14}Sn_4$	Ti—Sn
$Ti_{40}Zr_{10}Cu_{32}Pd_{14}Ga_4$	Ti—Ga
$Ti_{86}Al_{10}V_4$ (crystalline)	Ti64

2.2. Material Characterization

2.2.1. Structural and Morphological Analysis

The underlying microstructure and the degree of amorphousness of the BMGs were assessed in comparison to Ti64 using XRD (PANalytical X'Pert diffractometer, PANalytical, the Netherlands). Samples were measured continuously for 90 min in Bragg–Brentano configuration, using monochromated Cu Kα radiation ($\lambda = 0.15406$ nm) and a 2θ range of 20° to 90°. The XRD tube operated under an applied voltage of 45 kV and a current of 40 mA. For morphological analysis, cross-sectional lamellae of the samples were prepared using a Tescan Lyra focused-ion beam scanning electron microscope. TEM investigations were performed using a Thermo Scientific Titan Themis 200 G3 outfitted with a SuperX energy dispersive X-ray spectroscopy (EDX) detector to record elemental maps. All measurements were performed at 200 kV.

2.2.2. Thermal Stability Assessment

Thermal stability of the BMGs was assessed by performing isochronal differential scanning calorimetry (DSC) measurements (DSC1/700, Mettler-Toledo, USA) under a protective 6.0 argon-atmosphere gas flow. Samples with a weight range between 40 mg (for Ti-based alloys) and 350 mg (for Pt- and Pd-based alloys) were heated at a rate of 20 K min^{-1} from room temperature up to a maximum temperature of 732 K (Pd), 673 K (Pt), and 873 K (Ti, Ti—Sn, and Ti—Ga). The maximum temperature was kept lower than the melting point of the Al DSC pans, as well as under the melting point of the alloys.[29] After holding the maximum temperature for 5 min, the samples were cooled down at a rate of 20 K min^{-1}, and then re-heated to the maximum temperature. The glass transition temperature (T_g), crystallization temperature (T_x), and crystallization enthalpy (ΔH_x) were determined from the data using the software STARe (Mettler-Toledo); T_g and T_x were measured as the onset of the corresponding endothermic or exothermic events, respectively.

2.2.3. Mechanical Evaluation

Compression tests were performed at room temperature on rod samples with a diameter of 2 mm and length of 4 mm using a universal Schenck-Trebel RM 100 kN (Solingen, Germany) testing device, equipped with a Doli EDC580 controller, a Sandner EXA20-5 extensometer, and a Kistler piezoelectric load cell calibrated up to 60 kN. The upper and lower surfaces of the samples were ground flat and plan-parallel. The test was performed in track-control mode, using a strain rate ($d\epsilon/dt$) of 0.7×10^{-4} s^{-1}. The final stress–strain curves were corrected for the compliance of the device, and for a possible non-parallelism of the sample and/or machine plates. The Young's modulus was obtained from the slope of the linear part of the stress–strain curve. Five samples per BMG alloy were tested and all samples of identical composition behaved similarly.

2.2.4. Wettability Evaluation

The wettability of the BMGs and Ti64 was determined by carrying out water contact angle (WCA) measurements using a drop-shape analysis system (DSA100, Krüss GmbH, Germany). At room temperature, 1.5 µL of distilled water was dropped on the sample surfaces, and the WCA was determined using the ellipse tangent-1 method. Two samples per alloy were measured.

2.2.5. Surface Roughness Characterization

The surface roughness of polished BMG samples was characterized using atomic force microscopy (AFM) measurements. Deploying a Bruker Icon3 microscope equipped with a Bruker FESPA V2 tip (res. frequency 64 kHz, scan rate 0.3 Hz), three regions of interest were evaluated, each representing a 4×4 µm scan area.

2.3. Characterization of Blood–Material Interactions

2.3.1. BMG Incubation with Blood

Prior to commencing experiments, the BMGs were immersed in ethanol for 5 min and subsequently air dried. A standard venipuncture technique was used to collect whole blood from healthy male and female volunteers aged 18–55 years (ethical approval was obtained from the local ethics committee; BASEC Nr PB_2016_00816). The blood was partially heparinized in S-Monovette Tubes containing 3 IU mL^{-1} heparin to a final concentration of 0.5 IU mL^{-1}, and used within 1 h after withdrawal. Experiments were repeated with at least 3 different blood donors. The BMGs and Ti64 were incubated with blood in custom-made Teflon molds, as previously described.[30] Samples were incubated in blood for 8, 16, and 24 min, and subsequently washed with phosphate-buffered saline (PBS, Sigma, Switzerland) three times.

2.3.2. Scanning Electron Microscopy Analysis

The interaction of blood with BMGs in comparison to Ti64 was analyzed using scanning electron microscopy (SEM). Samples incubated with blood were fixed with Karnovsky solution (4% paraformaldehyde, 2.5% glutaraldehyde) for 1 h and washed twice with PBS. Afterward, samples were dehydrated in an increasing gradient of ethanol (EtOH) as follows: 50%, 70%, and

80% EtOH for 30 min; 90% and 100% EtOH for 60 min; and finally in hexamethyldisilazane (Sigma) for 30 min, and left to dry overnight. Samples were sputter-coated with a 5 nm layer of gold/palladium (EM ACE600, Leica Microsystems, Switzerland) before imaging at an accelerating voltage of 2.0 kV (Hitachi S-4800, Hitachi-High Technologies, Japan).

2.3.3. Confocal Laser Scanning Microscopy Analysis

Fibrin network formation on the surface of BMGs was assessed using confocal laser scanning microscopy (CLSM). BMG samples were fixed with 4% paraformaldehyde (4% PFA; 25 mM HEPES, 10 mM EDTA, 3 mM $MgCl_2$, 65 mM PIPES) for 30 min and then permeabilized with 0.1% Triton X (Sigma) for 30 min. Staining was performed with mouse anti-fibrinogen (1:200, ThermoFisher), followed by anti-mouse Alexa Fluor 555 (1:200, ThermoFisher). Imaging was carried out using an LSM 780 confocal microscope (Carl Zeiss AG, Switzerland). Image analysis of Z-stacks and their orthogonal views were applied to determine the thickness of the fibrin network on the surface of BMGs in comparison to Ti64 using ImageJ as previously described.[31]

2.4. Assessment of Cell–Material Interactions

2.4.1. Isolation of HBCs

Originating from patients undergoing hip replacement procedures, HBCs were isolated from the marrow of trabecular bone (ethical approval EKOS 22/193), as previously described.[32] HBC proliferation was stimulated in growth medium consisting of alpha-minimal essential medium (alpha-MEM; Gibco, Switzerland), 10% fetal calf serum (FCS; Lonza, Switzerland), 1% penicillin-streptomycin (P/S; Sigma), and 1 ng mL^{-1} basic fibroblast growth factor (Sigma), at 37 °C and 5% CO_2. HBCs were subcultured at a density of 2000 cells cm^{-2}, and all experiments were performed using at least 3 HBC donors, and cells of passage 2.

2.4.2. Cell Seeding

HBCs were seeded on 5 mm diameter BMG and Ti64 samples pre-incubated with human whole blood at a density of 20 000 cells cm^{-2}. Samples were cultured in 37 °C and 5% CO_2 with growth medium for 24 h to assess cell attachment, and for 28 days in osteogenic medium to evaluate mineralization by the cells on the surface. HBCs were stimulated to differentiate using osteogenic medium made up of alpha-MEM, 10% FCS, 1% P/S, 50 µM ascorbic acid (Sigma), 2 mM β-glycerol phosphate (Sigma), 10 nM 1,25-dihydroxy-vitamin D3 (Sigma), and 10 nM dexamethasone (Sigma). Vitamin D3 and dexamethasone were added freshly each time the osteogenic medium was changed, every 3–4 days.

2.4.3. Immunocytochemistry

The morphology of HBCs on the surface of BMGs and Ti64 was assessed via immunocytochemistry, and imaged using CLSM. After 24 h of incubation, samples were fixed and permeabilized as described in Section 2.3.2. The cell cytoskeleton was stained with Alexa Fluor 488-labeled phalloidin (1:200, ThermoFisher), while the fibrin network was stained with mouse anti-fibrinogen (1:200, ThermoFisher), followed by anti-mouse Alexa Fluor 555 (1:200, ThermoFisher). Cell nuclei were counterstained with 4',6-diamidino-2-phenylindole (DAPI; 1:1000, Sigma Aldrich). Imaging was carried out using an LSM 780 (Carl Zeiss AG).

2.4.4. Mineralization Assay

Mineralization was defined as the mass of calcium deposited by HBCs, normalized to the mass of DNA on a sample surface after 28 days of culture. Cells were lysed using 1 M hydrogen chloride (HCl) and solubilized calcium was then quantified with a Calcium Assay Kit KA4081 (Abnova Corporation, USA) following the manufacturer's protocol. Using separate samples, the total DNA content on the surface of BMGs and Ti64 was determined by lysing cells using a neutral pH buffer (150 mM NaCl, 1% Triton-X, 50 mM Tris-HCl) and then quantifying the DNA with the Quant-iT PicoGreen dsDNA Assay Kit (ThermoFisher), according to the manufacturer's instructions.

2.5. Evaluation of Antimicrobial Activity

2.5.1. Copper Release Kinetics

Inductively coupled plasma-optimal emission spectrometry (ICP-OES) measurements were carried out to determine the release kinetics of copper (Cu^{2+}) ions from the BMGs. Ti64 was included into the assay as a negative control and pure copper as a positive control. Samples were incubated in 2 mL of deionized water at 37 °C and 300 rpm (Thermomixer comfort, Eppendorf AG, Switzerland). After 1, 2, 3, and 7 days, the supernatant was collected and replaced with deionized water. Measurements were performed using the ICP-OES 5510 device (Agilent Technologies, USA) and analyzed with the software ICP Expert. The supernatant as well as the Cu^{2+} calibration standards, ranging from 0 to 5 ppm, were diluted with nitric acid. The results were normalized to the average mass of the sample.

2.5.2. Culture Maintenance of S. aureus

BMG antimicrobial activity was assessed using gram-positive *S. aureus* as it is the predominant pathogen responsible for causing osteomyelitis (bone infection).[33] *S. aureus* (ATCC 6538) was cultivated in 30% tryptic soy broth (TSB) medium (Sigma), supplemented with 0.25% glucose, and incubated at 37 °C and 160 rpm overnight. The concentration of bacteria in the pre-culture was determined by optical density (OD) at a wavelength of 600 nm using a Biophotometer Plus (Eppendorf, Switzerland) and subsequently diluted to an OD_{600nm} of 0.2 in fresh TSB medium. The bacterial suspension was subsequently incubated for another 90 min at 37 °C and 160 rpm to reach an exponential growth phase, and diluted with fresh TSB medium to an OD_{600nm} of 0.5. Finally, 100 µL of bacterial culture were spiral-plated on Plate-Count-Agar plates (easySpiral Pro, Interscience, France).

2.5.3. Agar Diffusion Assay and Touch Test

Agar diffusion assay and touch test were used to qualitatively assess the antimicrobial activity of BMGs and Ti64 against *S. aureus*. In the diffusion assay, samples were placed onto the bacterial lawn and incubated overnight at 37 °C. The zone of inhibition was assessed using a Scan 300 colony counter (Interscience, France). In the touch test, samples were removed from the bacterial lawn after 30 min, and the plates were incubated overnight at 37 °C. The area that the samples touched was checked for the presence of bacterial growth.

2.5.4. Colony Forming Unit Assay

A colony forming unit (CFU) assay was performed to quantify the antimicrobial activity of BMGs and Ti64 against *S. aureus*. 40 µL of bacteria (OD_{600nm} of 0.01 corresponding to $\approx 10^6$ CFU mL^{-1}) in 0.9% sodium chloride (NaCl) solution were placed on the surface of 5 mm diameter BMGs, Ti64, and pure copper. The samples were subsequently incubated at room temperature for 8 h and then washed twice with 200 µL 0.9% NaCl. The supernatant was collected. The samples were sonicated in 200 µL 0.9% NaCl for 5 min and vortexed for 15 s, and the suspension was collected. All supernatants were mixed and a serial dilution with 0.9% NaCl was performed. From each dilution, 20 µL were spotted in triplicate on PC-Agar plates, which were then incubated overnight at 37 °C. The number of CFU was counted and the data were analyzed using a Scan 300 colony counter.

2.5.5. Live/Dead Assay

A live/dead assay was carried out to assess the anti-fouling properties of the BMGs in comparison to Ti64. 20 µL of bacteria (OD_{600nm} of 0.01 corresponding to $\approx 10^6$ CFU mL^{-1}) were placed on the sample surfaces and covered with sterile parafilm. Samples were incubated for 24 h at 37 °C and subsequently washed with 200 µL 0.9% NaCl to remove non-adherent cells. Live/dead staining was carried out according to the BacLight Bacterial Viability kit's protocol (ThermoFisher). Samples were then washed twice with dH_2O, subsequently fixated in Karnovsky solution (4% PFA, 2.5% glutaraldehyde) for 30 min, and washed twice with 200 µL 0.9% NaCl. Images were taken with a fluorescent microscope (Leica DM6000, Germany).

2.6. Statistical Analysis

Results were expressed as mean ± standard deviation, unless otherwise stated. Analysis of the statistical significance between groups was performed by one-way analysis of variance (ANOVA) with Tukey post-hoc test, as indicated in each figure caption. In vitro results were obtained from experiments that were repeated at minimum three times, with different donors of blood and HBCs each time. For antimicrobial evaluation, the experiments were independently repeated three times. Additionally, within each experiment, 4 different technical replicates were used. Statistical analyses were performed using Prism 9 (GraphPad Software Inc., USA). Asterisks denote statistical significance as follows: * $p < 0.05$, ** $p < 0.01$, *** $p < 0.001$, and **** $p < 0.0001$.

Table 2. Summary of Pd-, Pt-, and Ti-based BMG DSC. Thermal properties of Pd, Pt, Ti, Ti—Ga, and Ti—Sn, including their glass transition temperature (T_g), crystallization temperature (T_x), supercooled liquid region ($\Delta T = T_x - T_g$), and enthalpy of crystallization (ΔH_x).

	Pd	Pt	Ti	Ti—Ga	Ti—Sn
Glass transition temperature (T_g), K	577	500	632	651	678
Crystallization temperature (T_x), K	586	565	705	713	733
Supercooled liquid region (ΔT), K	109	65	73	62	55
Enthalpy of crystallization (ΔH_x), kJ mol^{-1}	468	470	112	111	196

3. Results and Discussion

3.1. Thermal Stability

DSC analysis shows that all BMGs featured a single endothermic event, followed by a number of exothermic transitions from a glassy, disordered state to a devitrified, crystalline state— the first of which is highlighted in **Figure 1**A–E. The multistage crystallization events indicate a stepwise transformation from the amorphous to crystalline state. Generally, BMG thermal stability is associated with the broadness of the supercooled liquid region (SCLR), which is marked by the difference between crystallization temperature (T_x) and glass transition temperature (T_g). While all BMGs showed excellent glass-forming abilities, Pd is by far the best glass former with an at least 1.5-fold higher SCLR in comparison to Pt- and Ti-based BMGs (Ti, Ti—Ga, and Ti—Sn) (**Table 2**). The enthalpy of crystallization (ΔH_x) is proportional to the degree of amorphousness in a BMG, as more energy is required and thus released when crystalizing a greater volume fraction of amorphous material. The enthalpy of crystallization for Pd and Pt was found to be similar (468 and 470 kJ mol^{-1}, respectively), and in agreement with other reports.[34–37] The DSC data of Ti is also generally similar to that found in previous reports.[18,38] However, the glass transition temperature of Ti is markedly lower in comparison to previous studies, which may be due to the proximity to its critical casting thickness when preparing the samples. While the influence of Ga and Sn did not massively influence the SCLR, the addition of Sn led to a notable increase in the enthalpy of crystallization, with an at least 1.7-fold increase over Ti and Ti—Ga. This suggests that the critical casting thickness of Ti is improved by the addition of Sn, which is in agreement with previous studies.[27,38] Thus, while the addition of Ga might enhance the antimicrobial properties of Ti, the addition of Sn improves the glass-forming ability and therefore increases its potential range of applications.

3.2. Mechanical Properties

The Young's moduli of Pd (73 GPa) and Pt (68 GPa) samples were found to be similar (**Figure 2**A), while their mechanical behavior was quite different. Pd began to yield at a strain of 2% and underwent plastic deformation after initially showing elastic behavior, as expected for BMGs.[39] After yielding, the stress–strain

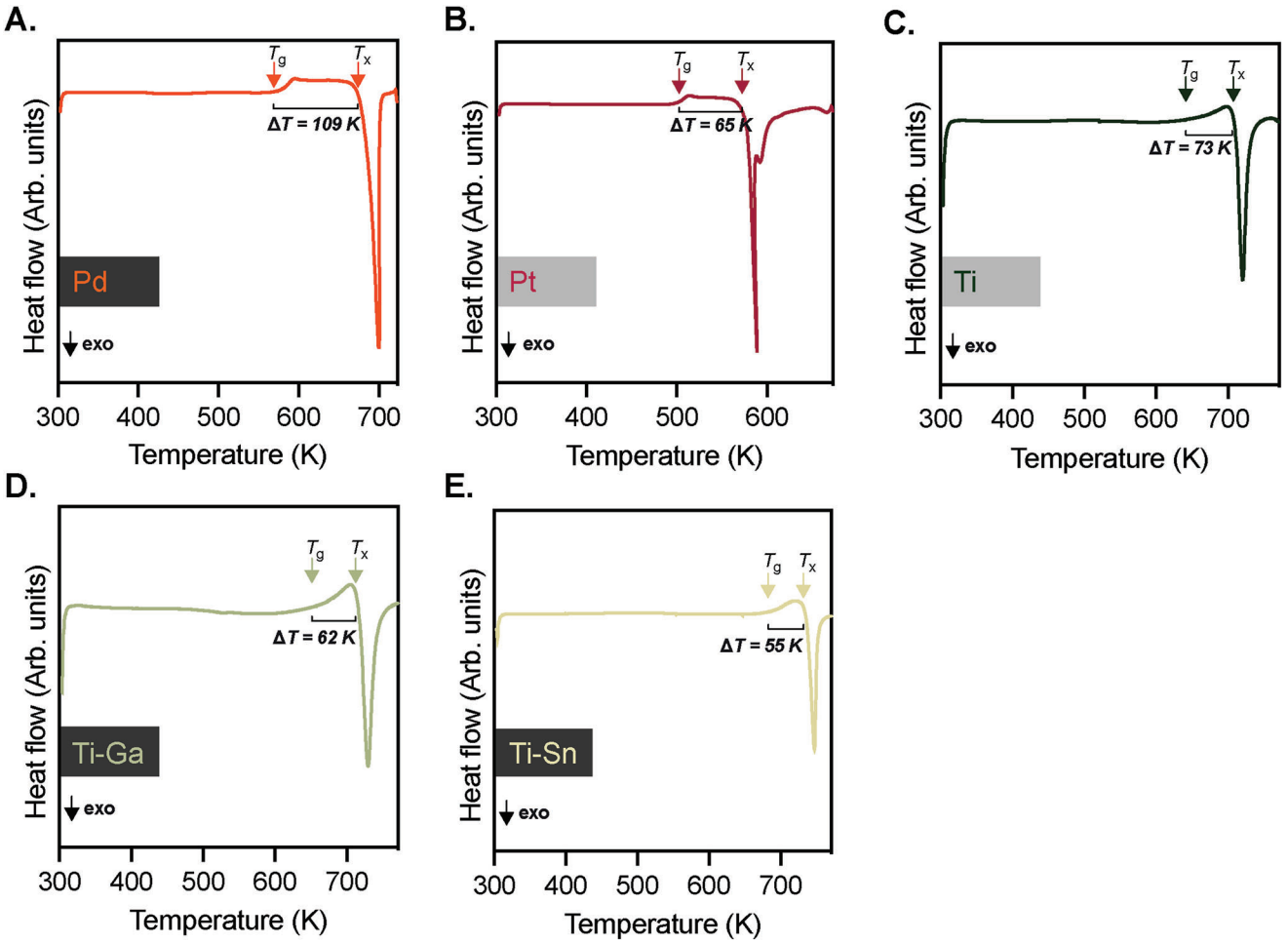

Figure 1. Glass-forming ability of Pd-, Pt- and Ti-based BMGs. A–E) Representative DSC data of Pd, Pt, Ti, Ti—Ga, and Ti—Sn, indicating their glass transition temperature (T_g), crystallization temperature (T_x), and supercooled liquid region (ΔT).

curve featured a number of serrations, resulting from shear-band formation and "stick-slip" shear banding typically observed in BMGs.[40] The average yield stress of Pd samples was 1525 MPa and the maximum stress attained during plastic deformation was 1561 MPa (Figure 2B). Following a brief period of plastic deformation (plastic strain of 0.2%), the Pd samples ultimately fractured under a compressive stress of 1548 MPa. Although there is limited data on the mechanical properties of $Pd_{43}Cu_{27}Ni_{10}P_{20}$, one previous report has assessed its mechanical behavior while bending.[41] However, comparing bending and compression tests should be done with caution as bending introduces the concomitant action of tensile and compressive loads. Additionally, the

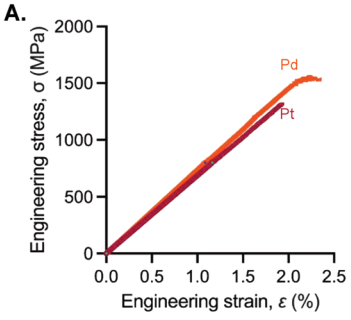

B.

Sample	Young's modulus E [GPa]	Yield stress σ_y [MPa]	Yield strain ε_y [%]	Maximum stress σ_{max} [MPa]	Fracture stress σ_f [MPa]	Fracture strain ε_f [%]
Pd	73	1525	2.12	1561	1548	2.28
Pt	68	--	--	1318	1318	1.92
Ti	78	1791	2.3	1896	1892	3.8
Ti-Ga	63	1622	2.6	1776	1772	4.7
Ti-Sn	72	1636	2.3	1776	1770	6.1

Figure 2. Mechanical properties of Pd-, Pt- and Ti-based BMGs. A) Stress–strain curves of Pd and Pt, illustrating the mechanical behavior of the BMGs under compression. B) Compressive mechanical properties of Pd, Pt, Ti, Ti—Ga, and Ti—Sn, including Young's modulus, yield stress, yield strain, maximum stress, fracture stress, and fracture strain. The data for Ti, Ti—Sn, and Ti—Ga were reproduced with permission [27] 2023, Elsevier.

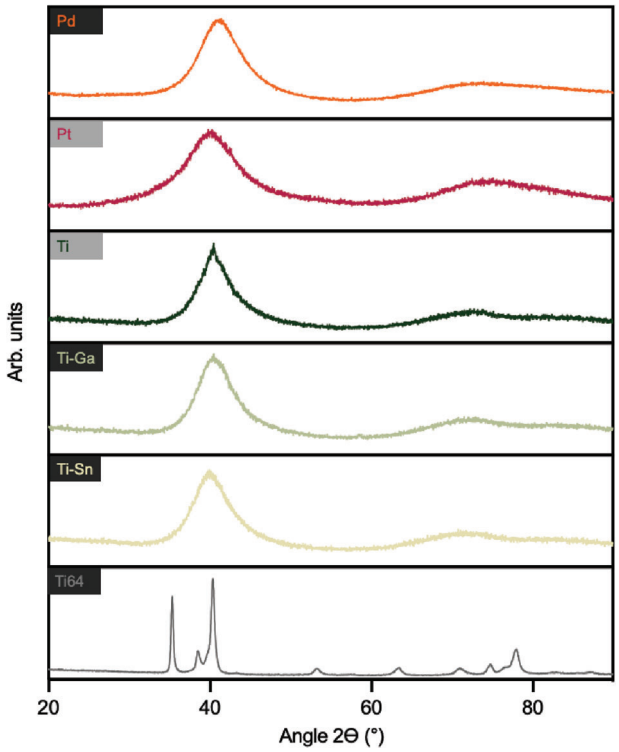

Figure 3. Amorphousness of BMGs. Representative X-ray diffraction (XRD) patterns of the BMGs investigated in this study in comparison to that of crystalline Ti64.

previous study produced samples of Pd using air-cooling and water-quenching, which is accompanied by different cooling rates,[41] and thus can promote the formation of amorphous structures with different degrees of relaxation, resulting in different mechanical behavior.[39] Bearing in mind the caveats of this comparison, the findings of this study are in agreement with the previously reported results, showing that Pd yields and then undergoes plastic deformation under pure compression.

In contrast, Pt did not show any plastic deformation under compressive load and fractured prematurely at a strain of <2%, which is below the typical value expected for BMGs. Moreover, while Pd exhibited fracture propagation along the maximum shear plane at 45°,[42] Pt fractured into many small pieces. This may be due to the presence of brittle nanocrystalline particles, which are unable to promote and deflect extensive shear-band formation.[39] Although the XRD pattern of Pt-based BMG (**Figure 3**) does not show any Bragg peaks, which would indicate the presence of crystalline phases, in-depth TEM analysis did reveal the presence of a small volume fraction of nanocrystallites embedded in an amorphous matrix (**Figure 4**A). Interestingly, a previously investigated Pt-based BMG ($Pt_{57.5}Cu_{14.7}Ni_{5.3}P_{22.5}$), which differs only marginally in composition from the Pt samples investigated in this study ($Pt_{57.4}Cu_{14.7}Ni_{5.3}P_{22.6}$), yielded at 2% strain under 1400 MPa compression and then deformed in a plastic manner, reaching a strain of almost 23% at fracture.[23] In contrast to the previously investigated Pt-based BMG, which reached a maximum stress under plastic deformation of 1470 MPa, the Pt in this study failed early with a fracture stress of 1318 MPa (Figure 2B). Despite this, the Young's moduli of the two Pt-based BMGs are similar (70 GPa [23] and 68 GPa, respectively), suggesting that the differences in mechanical behavior under applied load are caused by structural differences in the samples. These differences may originate from discrepancies in the sample preparation; Pt was prepared by direct suction of the molten alloy into Cu molds, while the previous study prepared $Pt_{57.5}Cu_{14.7}Ni_{5.3}P_{22.5}$ by water quenching.[23] Moreover, the master alloy in the previous study was flushed with B_2O_3 for 1200 s at 1000 K, a process that is known to improve glass-forming ability.[35,43,44]

The mechanical properties of the Ti-based BMGs (Ti, Ti—Ga, and Ti—Sn) have been investigated elsewhere,[27] and are included here for comparison (Figure 2B). The Ti-based BMGs featured more ductile behavior and plastic deformation in comparison to Pd and Pt. However, the ductility of Pd appears to depend on the cooling rates used during sample preparation, while nanocrystalline areas found in Pt account for an increase in brittleness. The Young's modulus of the Ti BMG decreased upon the addition of Ga and Sn (Ti: 78 GPa, Ti—Ga: 63 GPa, and Ti—Sn: 72 GPa), which can be explained by the lower Poisson ratios of Ga and Sn.[18] Additionally, it should be taken into consideration that the corrosion potential and passivity have been found to decrease when substituting 4 at% Cu with either Ga or Sn,[27] which may be attributed to structural relaxation occurring during rod casting.[45]

Upon proper annealing treatment, the mechanical properties of Ti64 reveal a compressive yield strength (as well as ultimate tensile strength) of 860 MPa, a Young's modulus of 114 GPa, and a relatively large tensile plastic deformation of 15%.[46] In comparison to Ti64, all currently investigated BMGs show greater potential to reduce stress shielding in orthopedic applications, albeit not eliminating it, with a Young's modulus that is at least 33% lower and only twice as high as that of human cortical bone. Moreover, the yield strain of all BMGs is more than double that of Ti64, indicating their capacity to withstand greater loads. However, an implant in a human body may be subjected to more complex loads including torsion, shear, tension, and compression, thus additional mechanical tests would be required to comment further on the biomechanics of these BMGs.

3.3. Structural and Morphological Characterization

The XRD pattern of all BMGs fitted the classical curve of amorphous materials, featuring two diffuse halos, resulting from the short-range order of the alloy, without well-defined Bragg peaks, as found in the graph of crystalline Ti64 (Figure 3). Upon closer examination, slight shifts of the broad maximum toward smaller diffraction angles were found when comparing Pt to Pd, and also when comparing Ti—Ga and Ti—Sn to Ti. Tuning the BMG composition leads to changes in the mean interatomic distance: Platinum has a bigger atomic radius (0.177 nm) in comparison to palladium (0.169 nm), while the bigger Ga (atomic radius of 0.135 nm) in Ti—Ga and Sn (atomic radius of 0.158 nm) in Ti—Sn replace the smaller Cu (atomic radius of 0.128 nm) atoms in Ti. The increase in interatomic distance may be responsible for the shift of the diffraction angle to lower values, as according to the

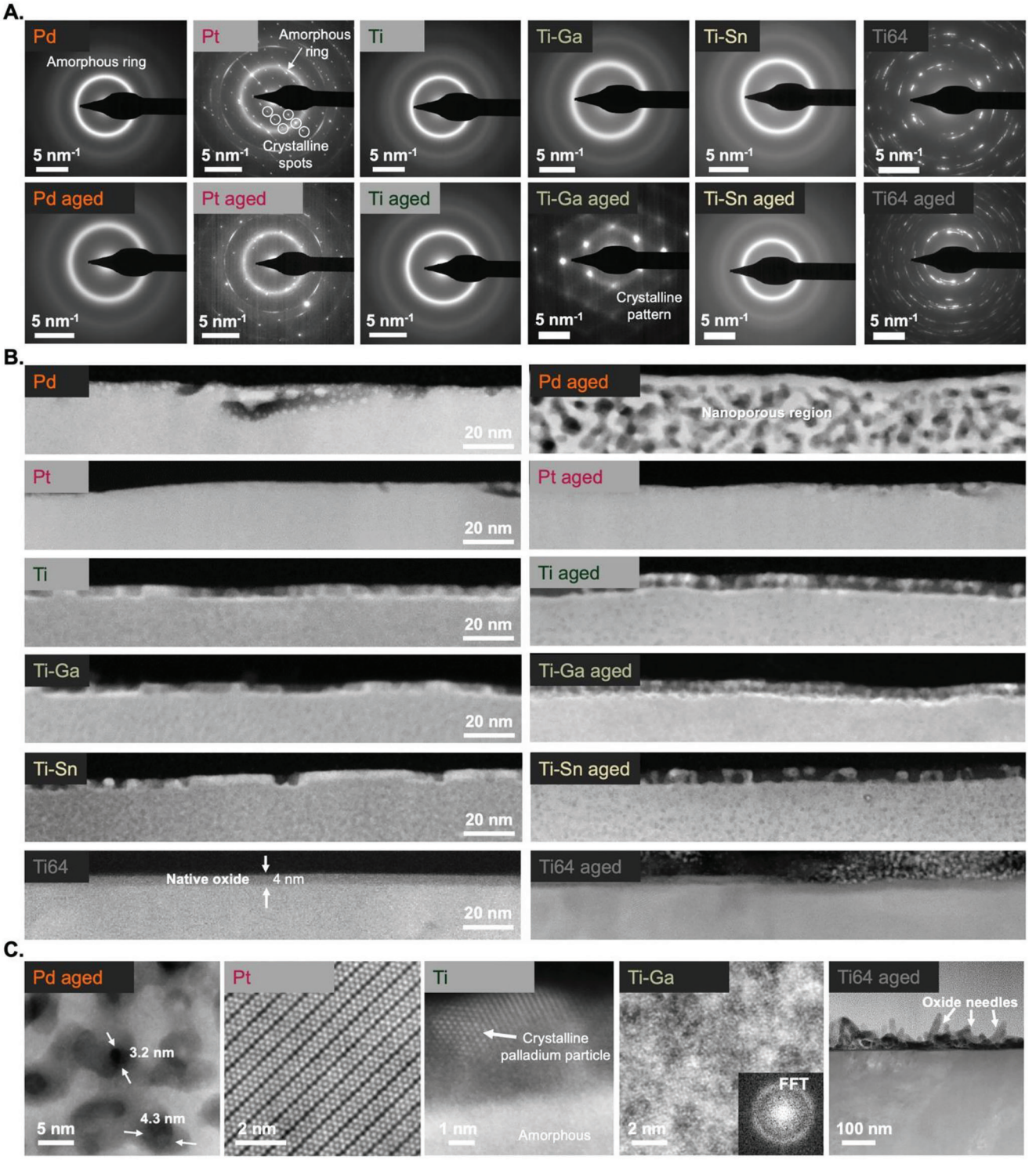

Figure 4. Stability of BMG surface morphology. A) Selected area diffraction patterns of the bulk region in BMGs and Ti64, showing amorphous rings, crystalline spots, and crystalline patterns. B) Cross-sectional high-angle annular dark field (HAADF) STEM images of the near-surface region showing the development of various surface morphologies across the different BMGs and Ti64. C) Highlighted features found across the different samples, including nanopores formed in Pd during aging, the nanostructure of crystals found in Pt, crystalline Pd droplets on the surface of Ti, the amorphous bulk of Ti—Ga (and corresponding Fast Fourier Transform image), and large TiO_2 needles formed on the surface of Ti64 during aging.

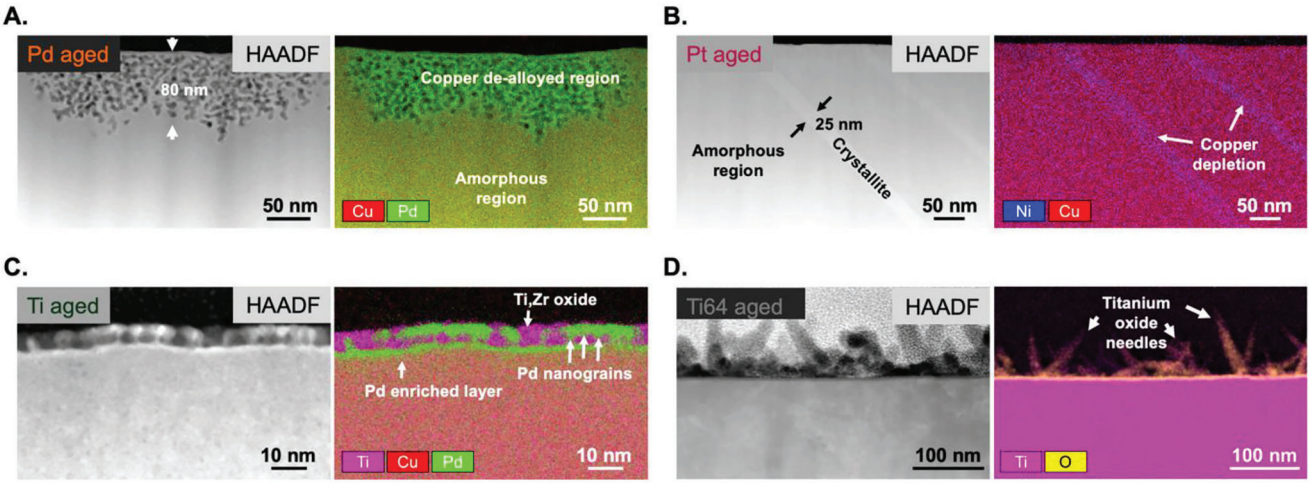

Figure 5. Chemical analysis of aged BMGs. Cross-sectional high-angle annular dark field (HAADF) images at various magnifications to optimally depict different specific features in A) Pd, B) Pt, C) Ti, and D) Ti64. The aged BMGs show distinct chemical enrichment and depletion at the near surface.

Ehrenfest equation and the definition of the wave vector, the 2θ angle is inversely proportional to the interatomic distance.[27]

The near-surface morphology and chemical stability of the BMGs was investigated using TEM, comparing as-prepared samples with samples aged in deionized water for 30 days at 37 °C. All BMGs were found to be amorphous in their as-prepared state as inferred from selected area electron diffraction (SAED) taken from the bulk region in the cross-sections, except for Pt (Figure 4A). Pt showed both a broad diffraction ring and sharp spots, indicating the presence of nanocrystalline areas within an amorphous matrix. After aging, all BMGs showed the same structure as before except for Ti—Ga, where a single-crystal-like pattern indicating the growth of micron-sized crystals was observed. Focusing on the near-surface morphology, different aging behaviors were observed depending on the BMG composition (Figure 4B). Pd featured an initially flat, mostly featureless surface with some minor local inconsistencies or surface defects, which may originate from the polishing procedure. However, a nanoporous network, which looks strikingly similar to the structures obtained by dealloying of metals,[47] developed at the surface during the aging process (Figure 4B left and right). The pore size in the aged Pd samples was in the range of 3–5 nm (Figure 4C). In contrast, Pt does not show such structures after aging and remains stable in its pristine form with a smooth, almost featureless surface (Figure 4B). Taking a closer look at the bulk region, crystalline slabs with a length of several hundred nanometers can be found embedded in the amorphous matrix (see **Figure 5**B), which explains the observed SAED pattern. The structure of these nanocrystals (Figure 4C) fits to the Pd_5TlAs-type structure,[48] which can be found in several Pt-based metal—phosphor compounds.[49,50]

The surface morphology of the Ti-based BMGs (Ti, Ti—Ga, and Ti—Sn) all show similar behavior during aging (Figure 4B). The surface layer was found to have a thickness of 5–8 nm, consisting of two segregated phases. After aging, the dual-phase structure is more refined with continuous parts of the brighter phase being broken up into smaller droplet-like features. Upon closer inspection, these features were identified as small face-centered cubic (fcc)-type crystallites embedded in an amorphous layer (Figure 4B,C). In contrast, the bulk part of all Ti-based BMGs was fully amorphous as inferred from high-resolution STEM (exemplary shown for as-prepared Ti—Ga) (Figure 4C). In alignment with the findings of this study, a recent report described the presence of a 15 nm-thick surface region composed of a mixed amorphous and nanocrystalline structure in $Ti_{40}Zr_{10}Cu_{36}Pd_{14}$.[14] Finally, the crystalline Ti64 sample featured a continuous native oxide layer with a thickness of 4 nm. After aging, this layer was still present but additional oxide structures had grown on the surface. These structures had a needle-like morphology with a length of up to 120 nm (Figure 4B,C). Taken together, despite some changes in morphology at their near-surface, the stability of Ti-based BMGs was found to be superior in comparison to that of Ti64 based on the sheer scale of the changes observed.

Elemental maps generated from EDX were used to further characterize selected samples after aging (Figure 5). While some changes in the near-surface morphology are depicted, Figure 5 highlights that the elemental distribution in all BMG samples is otherwise uniform and does not change significantly during aging. The nanoporous structure found in aged Pd samples reached depths of up to 100 nm, and showed an almost complete depletion of copper (Figure 5A). The remaining porous palladium structures have been shown to form in a similar BMG ($Pd_{30}Ni_{50}P_{20}$) using electrochemical de-alloying.[4] The crystals found in Pt were visible in the elemental map as a region of copper depletion in both the as-prepared and aged samples (Figure 5B showing the aged sample). The dual-phase structure of Ti, including Ti—Ga and Ti—Sn, consisted primarily of Ti, Zr oxide, and Pd, Cu droplets on top of a Pd-enriched layer (Figure 5C). The growth of the oxide phase and concurrent shrinkage of Pd, Cu regions during aging suggest that these elements are likely released during the aging process in a manner similar to a process previously observed by in situ synchrotron XRD.[51] In contrast, Ti64 shows the most significant changes during the aging process with a growth of up to 120 nm-long TiO needles (Figure 5D).

3.4. Blood–Material Interactions

Blood–material interactions are dependent on a spectrum of surface properties, including WCA, roughness, and surface chemistry.[30,52] A critical early step in the course of blood–material interactions is the adsorption of fibrinogen, which can regulate the adhesion of platelets, and modulate their activation, thereby contributing to fibrin clot formation.[53] The fibrin clot serves as a provisional matrix, which cells from the surrounding tissue use to initiate the process of integration. Implant affinity to blood proteins such as fibrinogen is linked to increased interactions with growth factors, attenuation of pro-inflammatory responses, and faster osseointegration.[54–56] While the Pd and Pt BMGs provided limited support for fibrin network formation in comparison to Ti64, the Ti-based BMGs supported faster and thicker fibrin network formation when in contact with human whole blood (**Figure 6**), despite crystalline Ti64 revealing a significantly lower water contact (Figure 6D). This suggests that WCA is not the main determinant of fibrin network formation on BMG surfaces. Among the surface properties that could have influenced this, it is likely that surface oxides (Figures 4 and 5), coupled with the release of ions from the surface (Figure 8, this aspect will be detailed later), are the main drivers that influence the rate of fibrin network formation, especially when considering that all samples in this study were polished equally and thus the contribution of surface roughness can be neglected S1 (Supporting Information). In line with this finding, minor adjustments to the chemical composition of Ti through the replacement of Cu by Ga and Sn, in Ti—Ga and Ti—Sn, led to significantly reduced fibrinogen deposition and fibrin network formation (Figure 6B). On the surface this appears to contradict the findings of another report, showing that the addition of 1% gallium to the composition of mesoporous bioactive glasses enhanced their support for blood-clot formation.[57] However, the same study[57] also showed that 3% gallium has the opposite effect, suggesting that the response of blood to BMGs is not only dependent on their chemical composition, but also on the concentration of the elements that make up their composition. This is further demonstrated in a recent report,[25] where a Pd-based BMG with a different chemical composition and elemental concentration, $Pd_{77.5}Si_{16.5}Cu_6$ as opposed to $Pd_{43}Cu_{27}Ni_{10}P_{20}$, revealed limited support for fibrin network formation, showing early signs of network formation only after 48 min of incubation with blood, whereas in this study the surface of Pd supported fibrin network formation by the 24-min mark (Figure 6A). Moreover, small changes to the chemical composition of the Ti BMG not only led to a marked change in the rate of fibrin network formation, but also to the WCA with Ti having a lower WCA than Ti—Ga and Ti—Sn (Figure 6D), which inversely correlates to the fibrin network thickness on the same BMGs (Figure 6C).

All BMGs were initially comparable with Ti64 when incubated with blood at the 8-min mark (Figure 6A), suggesting an initially similar blood–material interaction. Platelet attachment was supported across all surfaces. However, only Ti, Ti—Sn, and Ti64 supported fibrin network formation by the 16-min mark, whereas Pd, Pt, and Ti—Ga revealed limited fibrin network formation even after 24 min. Furthermore, the morphology of the fibrin network appeared denser (Figure 6B) and thicker (Figure 6C) on Ti, Ti—Sn, and Ti64 in comparison to Pd, Pt, and Ti—Ga. One possible explanation for this may be the differential adsorption of fibrinogen modulating the conformation of platelet attachment.[25] However, the platelet morphology across all surfaces was comparable, featuring a dendritic shape, long pseudopodia, and partial aggregation. This suggests that either the surface chemistry or ions being released from the surface might play a role in steering the fate of blood interactions with BMGs. It has previously been shown that the release of calcium ions from Ti surfaces can modulate blood–clot formation.[58] Calcium can modify the surface charge of titanium oxide and modulate protein adsorption, and platelet adhesion and activation, while also stimulating the production of alpha- and dense-granules. In this study, copper ions were released from all of the BMGs but to different degrees depending on the alloy's chemical composition (Figure 8A). Applying the same principle, it is possible that by a similar mechanism the differential release of copper ions influences the rate of fibrinogen adhesion and fibrin network formation. This is supported by previous reports, which show that copper ions have the capacity of increasing clotting time.[59,60] This might explain the difference in properties between Ti, which exhibits a low copper-ion release and enhanced fibrin network formation, and Pd, which exhibits a high copper ion release and limited fibrinogen adsorption. However, the low copper-ion release of Pt does not explain its limited fibrinogen adsorption. This suggests that chemical-ion release is likely a contributing factor influencing the rate of blood protein adhesion and fibrin network formation, while a vastly different surface chemistry is expected to be the determining factor influencing blood protein adhesion.

3.5. Mineralization

An implant's osseointegration capacity can be influenced by its mechanical properties; by its bioactivity, which can be defined by its capacity to steer the response of tissue-resident cells, for example by enhancing osteogenesis; and by its capacity to chemically bind free calcium and phosphate at the implant interface.[61–63] In this study, we assessed the capacity of BMGs to steer the osteogenic response of HBCs while taking into account the influence of blood–material interactions using a well-established in-vitro assay with enhanced physiological relevance.[32,64–66] The BMGs' capacity to support HBC attachment was comparable to that of Ti64 (**Figure 7**A). After only 24 h, HBCs had developed an elongated cell morphology and spread over the fibrinogen-decorated surface of BMGs and Ti64 (Figure 7A). The random spreading pattern of the cells suggests that the adsorption of fibrinogen to the surface was isotropic, providing a homogenous distribution of binding sites for HBCs. After 28 days, less DNA was found on the BMGs in comparison to Ti64, with significant differences observed between Pd, Pt, Ti—Ga, and Ti64 (Figure 7B). Additionally, the BMGs were found to markedly enhance mineralization in comparison to Ti64, with the same trend across three different HBC donors (Figure 7C). Mineralization, as denoted here, takes into account the absolute mass of calcium found on the sample surface, a well-established indicator of osteogenic phenotype, normalized to the amount of DNA. Previous studies have shown that the proliferation rate of bone progenitor cells can decrease as they commit in their differentiation to osteoblasts.[67] Taken together, these findings suggest that BMGs

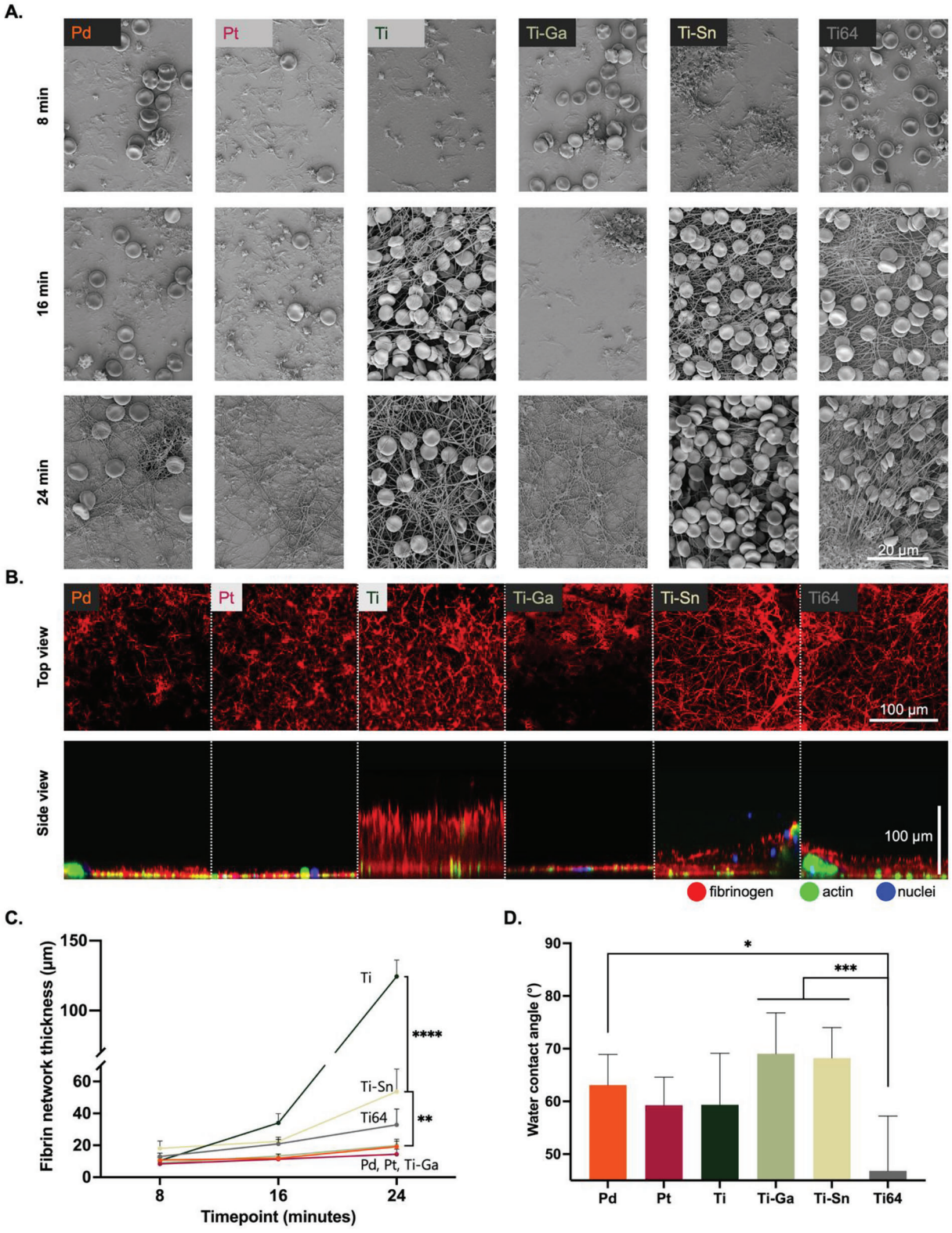

Figure 6. Influence of BMG composition on the dynamics of fibrin network formation. A) SEM images depicting the formation of a fibrin network on BMG and Ti64 surfaces after incubation with human whole blood for 8, 16, and 24 min. B) Top-view and orthogonal view of 24 min samples highlighting the structure and thickness of the fibrin network. C) Quantification of the fibrin network thickness. D) Water contact angle measurements of the BMGs and Ti64. $n = 6$; *, **, ***, **** denotes $p < 0.05$, $p < 0.01$, $p < 0.001$, and $p < 0.0001$; one-way ANOVA.

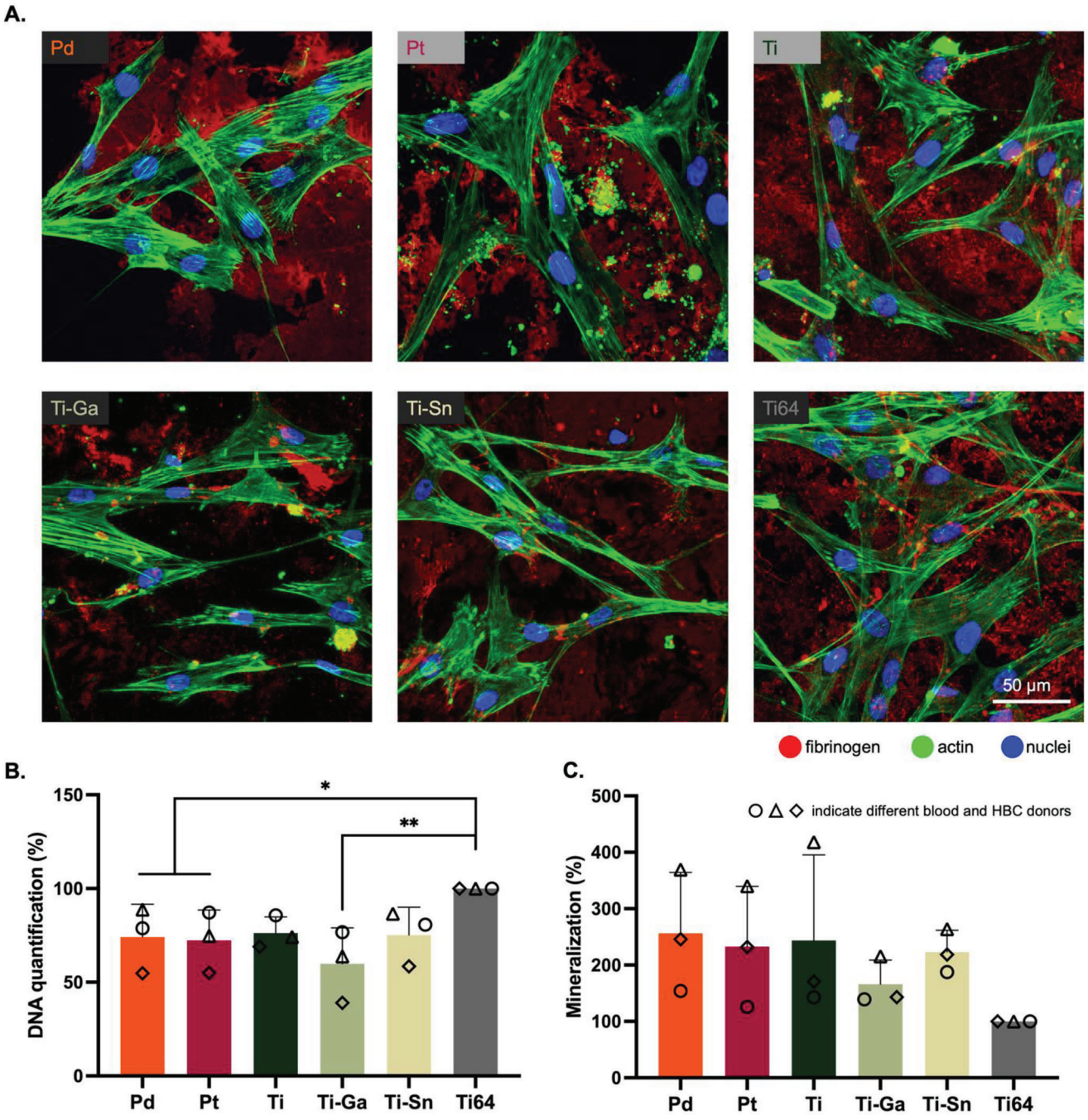

Figure 7. Influence of BMG composition on the mineralization capacity of HBCs. A) HBC morphology after 24 h on the surface of BMGs and Ti64 pre-incubated with blood. B) Total DNA quantity on the surface of BMGs and Ti64 after 28 days of culture in osteogenic medium. C) Mineralization on BMGs and Ti64 represented as the quantity of calcium normalized to the mass of DNA on the surface of each sample. $n = 3$; *, ** denotes $p < 0.05$ and $p < 0.01$; one-way ANOVA.

enhance osteogenesis by up to a factor of 2.5 in comparison to Ti64.

When assessing the influence of BMG's chemical composition on mineralization, the Pd and Pt BMGs performed similarly, while the addition of gallium and tin did not have a marked effect in comparison to the Ti BMG in this assay. Previous studies have shown that gallium ions can enhance the differentiation of bone progenitor cells.[68,69] However, such studies carried out their osteogenic assays in the absence of blood, while gallium ions were readily presented to bone progenitor cells as opposed to being released from an amorphous metallic alloy. In this study, gallium ions were detected in ICP-OES measurements at extremely low levels, representing 10% of the amount of Cu released (**Figure 8**A).

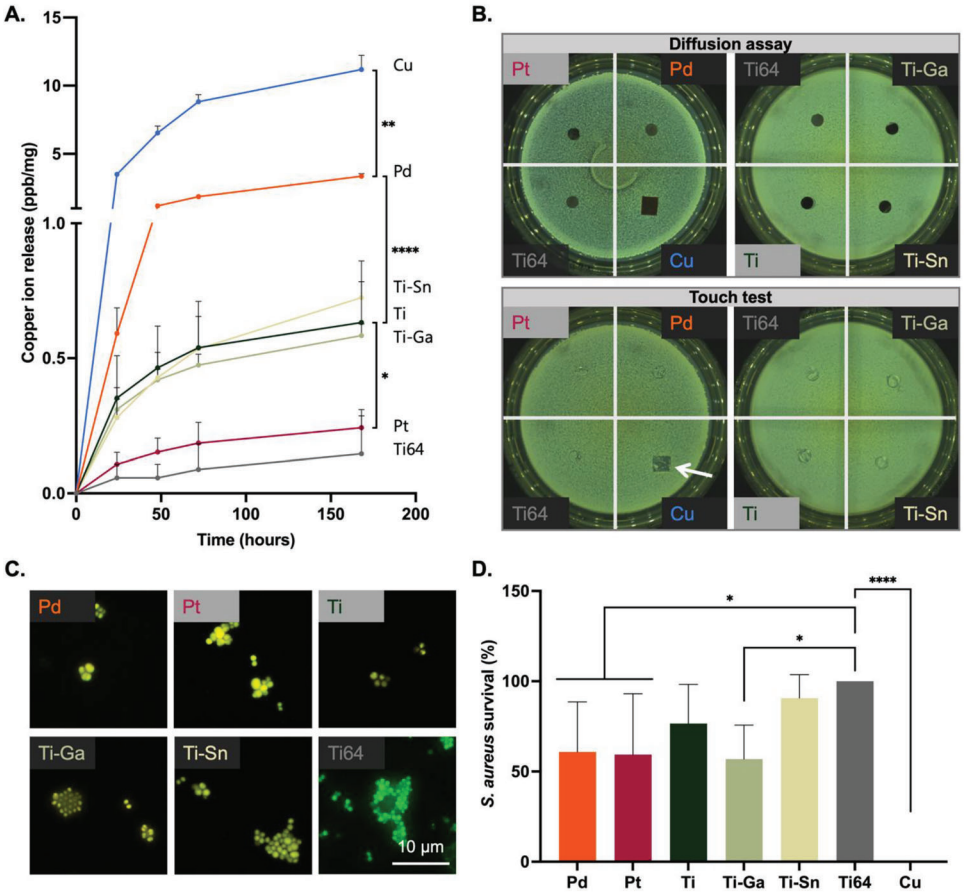

Figure 8. Influence of BMG composition on the antimicrobial activity against *S. aureus*. A) Copper-ion release from BMGs and Ti64 in deionized water. B) Antimicrobial diffusion assay and touch test showing only pure copper to exhibit a contact-killing effect against *S. aureus* (highlighted with arrow). C) Live bacteria fluoresce green and non-viable bacteria, permeable to propidium iodide, fluoresce yellow (merge of green and red). D) Colony forming unit assay showing the relative survival of *S. aureus* (relative to the survival on Ti64). $n = 3$; *, **** denotes $p < 0.05$ and $p < 0.0001$; one-way ANOVA.

The copper ions found to be released from the BMGs may be a contributing factor to the enhanced osteogenesis observed in BMGs, as other studies demonstrated the capacity of copper to enhance osteogenesis.[70] However, such studies typically investigate the influence of copper ions at much higher levels than the ones reported in this study. Bearing this in mind, it is also possible that the cell-culture medium could trigger enhanced copper-ion release,[71] or that the local concentration of copper ions at the interface with the BMG is higher than that of the bulk supernatant collected for the ICP-OES measurements.[72] Nevertheless, taking into consideration the superior mechanical properties of BMGs, coupled with their enhanced capacity to support osteogenesis, this study highlights the great potential of BMGs to support enhanced osseointegration in comparison to Ti64.

3.6. Antimicrobial Activity

Infection presents a significant challenge in orthopedic care, occurring predominantly following traumatic injuries and open fractures, where there is a breach in the skin allowing bacteria to enter the wound and colonize bone tissue. A much reduced, although not insignificant, risk of infection occurs during implant placement in the operating room. In either case, *S. aureus* colonization and biofilm formation are commonly associated with infection-related implant failure.[73,74] In the case of dental implants, the artificial surface of implants presents an opportunity for bacteria from the oral cavity to colonize and form a biofilm.[75] The first step of bacterial colonization is attachment to the implant surface. This has given rise to the so-called "race for the surface" between surrounding tissue cells for implant integration and bacterial cells for implant colonization. BMGs may be used to support surrounding tissue cells, while preventing bacterial cells from colonizing the implants.

In this study, BMGs were shown to elicit a sustained release of copper ions (Figure 8A). Notably, a caveat of this study is that the release of Cu ions was assessed in dH_2O for consistency with other material characterization, and not in a more physiological environment such as simulated body fluid, which could introduce some ion exchange and dissolution-precipitation reactions to take place. While such environments might enhance the level of ions released, it is expected that the trends of Cu release observed in dH_2O would remain. Copper has well-established concentration-dependent contact-killing and antimicrobial properties,[28] which have been confirmed by pure copper's ability to elicit antimicrobial activity in a touch test but not

in a diffusion assay (Figure 8B). The concentration of copper obtained from the ICP-OES measurements is orders of magnitude below the minimum inhibitory concentration of 250 ppm.[76] As expected, based on the copper levels observed, no inhibition zone was observed in the agar diffusion test with any of the BMGs (Figure 8B). A caveat of these assays is their limitation in permitting a more accurate measure of antimicrobial activity beyond a binary output. To further screen for antimicrobial activity, bacteria were directly cultured on the samples for 24 h and a superior anti-fouling effect was observed on the BMGs in comparison to Ti64 (Figure 8C). Additionally, the survival of *S. aureus* in a CFU assay was significantly reduced by up to 44% after exposure to Pd, Pt, and Ti—Ga for 8 h in comparison to Ti64 (Figure 8D). Notably, the Ti-based BMGs exhibited similar release of Cu ions—however, only Ti—Ga exhibited significant antimicrobial activity, suggesting that the extremely low amount of gallium released (10% that of Cu), together with the limited amount of copper release, contributed toward Ti—Ga's antimicrobial activity. These results are in line with previous findings that also showed gallium's potent antibacterial efficacy.[57] Taken together, these results suggest that the BMGs studied here have extended antimicrobial activity, which can be attributed at least in part to the release of copper (and gallium in the case of Ti—Ga) ions and the surface chemistry of each BMG. The low release of copper ions is also promising from the point of view of mitigating potentially toxic side effects usually associated with high-level release of antimicrobial compounds.

4. Conclusions and Outlook

In this study, BMGs with a wide range of glass-forming abilities were investigated. While the Pd-based BMG with its high glass-forming ability may be better suited for larger implants and some small prostheses, the Pt- and Ti-based BMGs may find use in smaller devices including implant screws and dental implants. The mechanical properties of BMGs were found to have great potential to reduce the capacity of inducing stress shielding in comparison to Ti64, while their deformation profile varies depending on the chemical composition and manufacturing process. Depending on their chemical composition, the BMGs showed a dynamic surface morphology. Notably, the surface morphology of all BMGs was more stable than that of Ti64. The chemical composition of the BMGs was also a crucial determinant of their capacity to support the adsorption of blood proteins. While all BMGs were found to be compatible with blood, only Ti- and Ti—Sn supported enhanced formation of a fibrin network in comparison to Ti64, while Pd-, Pt-, and Ti—Ga showed greater thrombogenic resistance. The osteogenic properties of all BMGs were found to be excellent, with markedly superior support for human bone progenitor cell mineralization in comparison to Ti64. Additionally, Pd, Pt, and Ti—Ga demonstrated excellent anti-fouling and antimicrobial capacity against *S. aureus*.

BMGs also exhibit Newtonian viscous flow between the glass transition temperature and the onset of crystallization, enabling them to deform homogeneously under low strain rate in a process known as thermoplastic forming.[77] This property could facilitate the production of implants with designer topographical features at both the micro- and nano-scale.[78] Ultimately, this could provide a more accurate alternative to stochastic processes currently used for the treatment of implant surfaces, including anodization, sandblasting, and acid-etching.[32,64] The introduction of surface features could be used to further improve the capacity of BMGs to enhance osteogenesis in comparison to Ti64, as demonstrated here in the absence of any topographical features and notable surface roughness. Furthermore, the introduction of specific nano-scale topographies could be used to further improve the antibacterial properties of BMG-based implants beyond the level reported here.[79] Finally, new compositions with increased glass-forming ability may yet be discovered to amplify the range of BMG applications in the biomedical field.

Supporting Information

Supporting Information is available from the Wiley Online Library or from the author.

Acknowledgements

The authors would like to thank Empa and ETH Zurich for funding. Support by the ETH+ initiative within the framework of SynMatLab (Laboratory for Multiscale Materials Synthesis and Hands-On Education) is particularly acknowledged. Dr. Martina Cihova is thanked for performing the AFM measurements.

Open access funding provided by ETH-Bereich Forschungsanstalten.

Conflict of Interest

The authors declare no conflict of interest.

Author Contributions

W.A.L. contributed to conceptualization, methodology, investigation, data curation, formal analysis, writing, review, and editing. R.W., E.P., P.S., and M.S. contributed to methodology, investigation, resources, data curation, formal analysis, writing, and review. F.Z. and Q.R. contributed to methodology, investigation, resources, and data curation. J.F.L. and M.R. contributed to conceptualization, methodology, data curation, supervision, writing, review, and editing.

Data Availability Statement

The data that support the findings of this study are available from the corresponding author upon reasonable request.

Keywords

antimicrobial surfaces, bulk metallic glasses, osteogenic, palladium, platinum, titanium

Received: February 21, 2023
Revised: July 3, 2023
Published online: July 14, 2023

[1] S. Ferraris, S. Spriano, G. Pan, A. Venturello, C. L. Bianchi, R. Chiesa, M. G. Faga, G. Maina, E. Vernè, *J. Mater. Sci.: Mater. Med.* **2011**, *22*, 533.

[2] J. C. M. Souza, M. Henriques, W. Teughels, P. Ponthiaux, J.-P. Celis, L. A. Rocha, *J. Bio- Tribo-Corros.* **2015**, *1*, 13.
[3] M. Kazemi, S. Ahangarani, M. Esmailian, A. Shanaghi, *Surf. Coat. Technol.* **2020**, *397*, 126044.
[4] J. Yu, Y. Ding, C. Xu, A. Inoue, T. Sakurai, M. Chen, *Chem. Mater.* **2008**, *20*, 4548.
[5] L. Y. Watanabe, S. N. Roberts, N. Baca, A. Wiest, S. J. Garrett, R. D. Conner, *Mater. Sci. Eng., C* **2013**, *33*, 4021.
[6] P. Meagher, E. D. O'Cearbhaill, J. H. Byrne, D. J. Browne, *Adv. Mater.* **2016**, *28*, 5755.
[7] D. Apostu, O. Lucaciu, C. Berce, D. Lucaciu, D. Cosma, *J. Int. Med. Res.* **2018**, *46*, 2104.
[8] M. Kaur, K. Singh, *Mater. Sci. Eng., C* **2019**, *102*, 844.
[9] M. Martínez-Pérez, A. Conde, M.-A. Arenas, I. Mahíllo-Fernandez, J.-J. de-Damborenea, R. Pérez-Tanoira, C. Pérez-Jorge, J. Esteban, *Colloids Surf., B* **2019**, *173*, 876.
[10] A. G. Gristina, *Science* **1987**, *237*, 1588.
[11] S. M. Shiels, L. H. Mangum, J. C. Wenke, *Eur. Cells Mater.* **2020**, *39*, 77.
[12] G. M. Esteves, J. Esteves, M. Resende, L. Mendes, A. S. Azevedo, *Antibiotics* **2022**, *11*, 235.
[13] S. Bohara, J. Suthakorn, *Biomater. Res.* **2022**, *26*, 26.
[14] A. Rezvan, E. Sharifikolouei, A. Lassnig, V. Soprunyuk, C. Gammer, F. Spieckermann, W. Schranz, Z. Najmi, A. Cochis, A. C. Scalia, L. Rimondini, M. Manfredi, J. Eckert, B. Sarac, *Mater. Today Bio* **2022**, *16*, 100378.
[15] L. Shao, J. Ketkaew, P. Gong, S. Zhao, S. Sohn, P. Bordeenithikasem, A. Datye, R. M. O. Mota, N. Liu, S. A. Kube, Y. Liu, W. Chen, K. Yao, S. Wu, J. Schroers, *Materialia* **2020**, *12*, 100828.
[16] T. Wang, Y. D. Wu, J. J. Si, Y. H. Cai, X. H. Chen, X. D. Hui, *Mater. Sci. Eng., A* **2015**, *642*, 297.
[17] M. Calin, A. Gebert, A. C. Ghinea, P. F. Gostin, S. Abdi, C. Mickel, J. Eckert, *Mater. Sci. Eng., C* **2013**, *33*, 875.
[18] S. Bera, P. Ramasamy, D. Şopu, B. Sarac, J. Zálešák, C. Gammer, M. Stoica, M. Calin, J. Eckert, *J. Alloys Compd.* **2019**, *793*, 552.
[19] N. Chen, L. Martin, D. V. Luzguine-Luzgin, A. Inoue, *Materials* **2010**, *3*, 5320.
[20] J. F. Löffler, *Intermetallics* **2003**, *11*, 529.
[21] A. S. Inoue, N. Nishiyama, H. Kimura, *Mater. Trans., JIM* **1997**, *38*, 179.
[22] S. L. Zhu, X. M. Wang, F. X. Qin, A. Inoue, *Mater. Sci. Eng., A* **2007**, *459*, 233.
[23] J. Schroers, W. L. Johnson, *Phys. Rev. Lett.* **2004**, *93*, 255506.
[24] S. Cardinal, J. Qiao, J.-M. Pelletier, H. Kato, *Intermetallics* **2015**, *63*, 73.
[25] M. Cihova, E. Müller, Y. Chandorkar, K. Thorwarth, G. Fortunato, K. Maniura-Weber, J. F. Löffler, M. Rottmar, *Adv. Funct. Mater.* **2022**, *32*, 2108256.
[26] A. M. Loye, H.-K. Kwon, D. Dellal, R. Ojeda, S. Lee, R. Davis, N. Nagle, P. G. Doukas, J. Schroers, F. Y. Lee, T. R. Kyriakides, *Biomed. Mater.* **2021**, *16*, 045018.
[27] A. Lachová, M. Stoica, Š. Michalik, P. F. Gostin, M. Fujioka-Kobayashi, B. Schaller, J. F. Löffler, P. Sovák, *J. Alloys Compd.* **2023**, *940*, 168776.
[28] M. Vincent, R. E. Duval, P. Hartemann, M. Engels-Deutsch, *J. Appl. Microbiol.* **2018**, *124*, 1032.
[29] F. Haag, R. Sauget, G. Kurtuldu, S. Prades-Rödel, J. E. K. Schawe, A. Blatter, J. F. Löffler, *J. Non-Cryst. Solids* **2019**, *521*, 119120.
[30] W. A. Lackington, L. Fleyshman, P. Schweizer, Y. Elbs-Glatz, S. Guimond, M. Rottmar, *Mater. Today Bio* **2022**, *15*, 100303.
[31] C. A. Schneider, W. S. Rasband, K. W. Eliceiri, *Nat. Methods* **2012**, *9*, 671.
[32] B. S. Kopf, A. Schipanski, M. Rottmar, S. Berner, K. Maniura-Weber, *Acta Biomater.* **2015**, *19*, 180.
[33] E. A. Masters, B. F. Ricciardi, K. L. de M Bentley, T. F. Moriarty, E. M. Schwarz, G. Muthukrishnan, *Nat. Rev. Microbiol.* **2022**, *20*, 385.
[34] Y. Kawazoe, U. Carow-Watamura, D. V. Louzguine, in *Phase Diagrams and Physical Properties of Nonequilibrium Alloys*, Vol. *37C3* (Ed: U. Carow-Watamura), Springer, Germany **2019**.
[35] H. W. Kui, A. L. Greer, D. Turnbull, *Appl. Phys. Lett.* **1984**, *45*, 615.
[36] N. Nishiyama, M. Matsushita, A. Inoue, *Scr. Mater.* **2001**, *44*, 1261.
[37] I.-R. Lu, G. Wilde, G. P. Görler, R. Willnecker, *J. Non-Cryst. Solids* **1999**, *250–252*, 577.
[38] S. L. Zhu, X. M. Wang, A. Inoue, *Intermetallics* **2008**, *16*, 1031.
[39] J. F. Löffler, A. A. Kündig, F. H. dalla Torre, (Eds: J. R. Groza, J. F. Shackelford, E. J. Lavernia, M. T. Powers), CRC Press, **2007**, pp. 17.
[40] R. Maass, J. F. Löffler, *Adv Funct. Mater.* **2015**, *25*, 2353.
[41] G. Kumar, S. Prades-Rodel, A. Blatter, J. Schroers, *Scr. Mater.* **2011**, *65*, 585.
[42] J. X. Zhao, R. T. Qu, F. F. Wu, Z. F. Zhang, B. L. Shen, M. Stoica, J. Eckert, *J. Appl. Phys.* **2009**, *105*, 103519.
[43] D. Granata, E. Fischer, V. Wessels, J. F. Löffler, *Appl. Phys. Lett.* **2015**, *106*, 011902.
[44] D. Granata, E. Fischer, V. Wessels, J. F. Löffler, *Acta Mater.* **2014**, *71*, 145.
[45] Q. Wei, P. F. Gostin, O. Addison, D. Reed, M. Calin, S. Bera, P. Ramasamy, A. Davenport, *J. Electrochem. Soc.* **2019**, *166*, C485.
[46] ASM Aerospace Specification Metals Inc., Technical Data Sheet for Titanium Ti-6Al-4V (Grade 5), ELI, Annealed, https://asm.matweb.com/search/SpecificMaterial.asp?bassnum=MTP643, (accessed: January 2023).
[47] Y. Ding, M. Chen, *MRS Bull.* **2009**, *34*, 569.
[48] M. El-Boragy, K. Schubert, Z. Metallkde. **1970**, *61*, 579.
[49] E. Yu. Zakharova, S. M. Kazakov, A. Götze, H. Kohlmann, A. N. Kuznetsov, *J. Solid State Chem.* **2018**, *265*, 266.
[50] E. Yu. Zakharova, E. O. Dobroljubov, S. M. Kazakov, V. N. Khrustalev, A. N. Kuznetsov, *J. Solid State Chem.* **2019**, *276*, 217.
[51] P. F. Gostin, O. Addison, A. P. Morrell, Y. Zhang, A. J. M. C. Cook, A. Liens, M. Stoica, K. Ignatyev, S. R. Street, J. Wu, Y.-L. Chiu, A. J. Davenport, *Adv. Healthcare Mater.* **2018**, *7*, 1800338.
[52] L. Zhang, B. Casey, D. K. Galanakis, C. Marmorat, S. Skoog, K. Vorvolakos, M. Simon, M. H. Rafailovich, *Acta Biomater.* **2017**, *54*, 164.
[53] B. Furie, B. C. Furie, *N. Engl. J. Med.* **2008**, *359*, 938.
[54] M. A. Alfarsi, S. M. Hamlet, S. Ivanovski, *J. Biomed. Mater. Res., Part A* **2014**, *102*, 60.
[55] F. Schwarz, M. Wieland, Z. Schwartz, G. Zhao, F. Rupp, J. Geis-Gerstorfer, A. Schedle, N. Broggini, M. M. Bornstein, D. Buser, *J. Biomed. Mater. Res., Part B* **2009**, *88*, 544.
[56] L. Parisi, A. Toffoli, M. Cutrera, M. G. Bianchi, S. Lumetti, O. Bussolati, G. M. Macaluso, *Nanomaterials* **2019**, *9*, 1407.
[57] S. Pourshahrestani, E. Zeimaran, N. Adib Kadri, N. Gargiulo, S. Samuel, S. V. Naveen, T. Kamarul, M. R. Towler, *J. Mater. Chem. B* **2016**, *4*, 71.
[58] E. Anitua, R. Prado, G. Orive, R. Tejero, *J. Biomed. Mater. Res., Part A* **2015**, *103*, 969.
[59] E. A. Abou-Shady, H. E. Farrag, N. A. el-Damarawy, F. A. Mohamed, A. M. Kamel, A. A. Massoud, *J. Egypt. Public Health Assoc.* **1991**, *66*, 21.
[60] E. Jelis, D. Kristol, R. R. Arora, C. R. Spillert, 2004, 127, Paper presented at Proceedings of the IEEE 30th Annual Northeast Bioengineering Conference, Springfield, MA, United States.
[61] Y. Maazouz, G. Chizzola, N. Döbelin, M. Bohner, *Biomaterials* **2021**, *275*, 120912.
[62] L. Damiati, M. G. Eales, A. H. Nobbs, B. Su, P. M. Tsimbouri, M. Salmeron-Sanchez, M. J. Dalby, *J. Tissue Eng.* **2018**, *9*, 204173141879069.

[63] W. A. Lackington, D. Gehweiler, E. Zhao, I. Zderic, D. Nehrbass, S. Zeiter, A. González-Vázquez, F. J. O'Brien, M. J. Stoddart, K. Thompson, *Acta Biomater.* **2022**, *149*, 189.
[64] W. A. Lackington, P. Schweizer, M. Khokhlova, C. Cancellieri, S. Guimond, A.-L. Chopard-Lallier, J. Hofstetter, P. Schmutz, X. Maeder, M. Rottmar, *Adv. Mater. Interfaces* **2022**, *9*, 2201164.
[65] N. Ackerl, A. H. Bork, R. Hauert, E. Müller, M. Rottmar, *Appl. Surf. Sci.* **2021**, *545*, 149020.
[66] M. Rottmar, E. Müller, S. Guimond-Lischer, M. Stephan, S. Berner, K. Maniura-Weber, *Dent. Mater.* **2019**, *35*, 74.
[67] A. Infante, C. I. Rodríguez, *Stem Cell Res. Ther.* **2018**, *9*, 244.
[68] A. Rodríguez-Contreras, D. Torres, J. Guillem-Marti, P. Sereno, M. P. Ginebra, J. A. Calero, J. M. Manero, E. Rupérez, *Surf. Coat. Technol.* **2020**, *403*, 126381.
[69] M. Yu, Y. Wang, Y. Zhang, D. Cui, G. Gu, D. Zhao, *Mol. Med. Rep.* **2020**, *22*, 2741.
[70] Z. Lin, Y. Cao, J. Zou, F. Zhu, Y. Gao, X. Zheng, H. Wang, T. Zhang, T. Wu, *Mater. Sci. Eng., C* **2020**, *114*, 111032.
[71] J. Hedberg, H. L. Karlsson, Y. Hedberg, E. Blomberg, I. Odnevall Wallinder, *Colloids Surf., B* **2016**, *141*, 291.
[72] M. C. Cortizo, M. F. Lorenzo de Mele, *Biol. Trace Elem. Res.* **2004**, *102*, 129.
[73] S.-G. Woo, S.-Y. Lee, S.-M. Lee, K.-H. Lim, E.-J. Ha, Y.-B. Eom, *Folia Microbiol.* **2017**, *62*, 157.
[74] W. A. Lackington, K. Thompson, in *Racing for the Surface: Antimicrobial and Interface Tissue Engineering* (Eds: B. Li, T. F. Moriarty, T. Webster, M. Xing), Springer, Cham **2020**, pp. 225–243.
[75] A. Minkiewicz-Zochniak, S. Jarzynka, A. Iwańska, K. Strom, B. Iwańczyk, M. Bartel, M. Mazur, A. Pietruczuk-Padzik, M. Konieczna, E. Augustynowicz-Kopeć, G. Olędzka, *Materials* **2021**, *14*, 2030.
[76] A. Reyes-Jara, N. Cordero, J. Aguirre, M. Troncoso, G. Figueroa, *Front. Microbiol.* **2016**, *7*, 626.
[77] S. Bera, B. Sarac, S. Balakin, P. Ramasamy, M. Stoica, M. Calin, J. Eckert, *Mater. Des.* **2017**, *120*, 204.
[78] N. Li, J. Pan, Z. Liu, L. Liu, *Mater. Today Adv.* **2022**, *15*, 100253.
[79] S. Wu, F. Zuber, K. Maniura-Weber, J. Brugger, Q. Ren, *J. Nanobiotechnol.* **2018**, *16*, 20.